Applied Physics B (2024) 130:179
https://doi.org/10.1007/s00340-024-08319-5

RESEARCH

Detailed theoretical analysis on nonlinear dynamic characteristics of tunable photonic spiking neuron based on optically pumped Spin-VCSEL

Mei-Ling Zou[1] · **Xin-Hong Jia**[1] · **Wei-Jie Song**[1] · **Sha-Sha Deng**[1] · **Ming-Yu Bao**[1] · **Yu-Quan Tang**[1] · **Jiang-Tao Lv**[1] · **Xuan Zhang**[1]

Received: 12 April 2024 / Accepted: 6 September 2024

Abstract

In this article, we proposed the use of optically pumped spin vertical-cavity surface-emitting laser (Spin-VCSEL) to create a photonic spiking neuron. We studied the dynamics of excitability and inhibitability under optical injection and analyzed the propagation characteristics of spiking information between unidirectionally-coupled Spin-VCSEL neurons. Our results demonstrated that by properly selecting parameters such as negative disturbance intensity from stimulus, pump ellipticity, and frequency detuning, Spin-VCSEL can achieve repeatable spiking output mode. Additionally, under certain conditions, it is possible to achieve inhibitory spiking output by selecting positive disturbance intensity from stimulus. By adjusting the duration and intensity of the disturbance, we can obtain controllable spiking responses for both excitable and inhibitory neurons. Furthermore, we found that under optimized injection strength, the spiking signal from the transmitter of Spin-VCSEL can be successfully propagated to the cascaded receiver with high quality. This work is meaningful because Spin-VCSEL offers new control dimensions such as pump ellipticity. Therefore, our study provides a valuable new choice for neuron construction of photonic spiking neural networks (PSNN).

1 Introduction

With the rapid development of photonic integrated devices, ultrafast photonic spiking neural networks (PSNN) have been realized using integrated photonic nonlinear devices. This advancement provides a new approach to realize neuromorphic computing (i.e., brain-inspired computing) [1–4]. PSNN exhibit sub-nanosecond response times, enabling operation speeds up to 9 orders of magnitude faster than biological neuromorphic computation. Additionally, PSNN require lower power consumption similar to biological neurons as it only operates when pulse events occur [1–32]. Consequently, PSNN has garnered significant attention in the field of brain-inspired computing. Currently, research on PSNN primarily focuses on studying the properties of photonic neurons and exploring the network construction and training methods.

Research on PSNN neurons has reported a variety of structures that utilize nonlinear photonic components as biomimetic neurons [1–32]. These include graphene saturable absorption lasers [5], micro-disk lasers [6], two-section semiconductor lasers (SL) [7, 8], silicon-based micro-ring resonators (MRR) [9–11], micro-pillar lasers [12], and vertical-cavity surface-emitting lasers (VCSEL) [15–32]. In particular, VCSELs offer unique advantages such as lower threshold power, single longitudinal-mode lasing, rich polarization dynamics, easy coupling to optical fibers, and straightforward integration into two-dimensional arrays [15–24]. As a result, the use of VCSELs as spiking neurons has been widely studied in recent years. Their characteristics including leaky-integrate-and-fire (LIF) properties [15–23], excitability [15–18], inhibitability [19], reproducibility, controllability and spiking propagation [20, 21], are similar to those of biological neurons. A study by A. Hurtado et al.., which involved experimentally injecting orthogonal polarization pulse into VCSELs found that, under certain conditions of injection strength and frequency detuning, the

---

✉ Xin-Hong Jia
jiaxh_0@sicnu.edu.cn

[1] School of Physics and Electronic Engineering, Sichuan Normal University, Chengdu 610101, China

orthogonal output exhibited phasic and tonic spiking due to polarization switching and frequency beating [15]. Subsequently S. Y.Xiang et al.. numerically analyzed how system parameters influenced the characteristics of spiking neurons for this structure. They discovered serious relaxation oscillation (RO) in the tail of the spiking train [16]. Two solutions have been proposed: one is introducing a continuous component in orthogonal polarization and a pulse component in parallel polarization, in order to realize the transition between two injection-locked states (phasic pulse), or the transition from injection-locked state to beating effect between two injected fields (tonic pulse) [17]. The other one is applying negative external stimulus pulse on the continuous wave with orthogonal polarization optical injection, so that the output enters partial locking and experiences spiking excitation [18]. T. Deng et al.. demonstrated that latter solution exhibits good controllability repeatability and propagation characteristics [20, 21]. Y. Lu et al.. proposed a frequency-switched VCSEL neuron which experimentally obtained stable spiking response up to 1 Gbps [22]. Additionally, it was found that VCSEL with saturable absorption also displays high-quality spiking neuron characteristics [23–27].

In terms of PSNN network research, since 2018, S. Y. Xiang et al.. realized the unsupervised training of single-hidden layer PSNN composed of multiple VCSEL-SAs based on spike-timing-dependent plasticity (STDP) rules [24]. They also used the supervised training for the single-hidden layer VCSEL-PSNN based on STDP, anti-STDP and remote supervised method (ReSuMe) [25]. The VCSEL-SA-based PSNN was further applied to digital recognition, and good accuracy was achieved [26]. In 2021, the simultaneous adjustment of delay and weight was proposed, which effectively reduced the number of training times, and was successfully used for the classification tasks with accuracy greater than 92% [27]. In 2023, the characteristics of spiking neurons based on Fabry-Perot semiconductor laser (FP-SL) with saturable absorption regions were experimentally studied and used for image recognition [28]. Based on a single VCSEL neuron, image edge detection with high accuracy has been obtained [29, 30]. The XOR task was also performed in a single VCSEL-SA [31]. In 2022, Y. Lu et al.. proposed a delay-weighted PSNN architecture constructed by cascaded frequency and intensity switch VCSEL, which can generate spiking delay up to 60 ns, and was utilized for classification tasks with accuracy of $>90\%$ [32].

Compared to traditional VCSELs, Spin-VCSELs exhibit certain advantages. They demonstrate threshold reduction under certain conditions [33, 34], and the polarization state of the laser output can be manipulated by controlling pumping ellipticity (resulting in close-to-unity lasing output ellipticity) [35–37]. By manipulating physical parameters, Spin-VCSELs can also exhibit circularly polarized switching and bistability [38–40]. One notable advantage of Spin-VCSELs is their potential for ultra-high polarization oscillation frequencies, which can overcome the modulation bandwidth limitations observed in traditional VCSELs due to RO [41–43]. The use of strain to increase birefringence effects has been reported to achieve spin-polarized modulation (SPM) bandwidths up to 200 GHz [42, 43]. Regarding the nonlinear dynamics of Spin-VCSELs, N. Q. Li et al.. conducted a numerical analysis on parameter dependencies for stable regions of both left circular polarization (LCP) and right circular polarization (RCP) components, and discussed the characteristics of chaos communication based on Spin-VCSEL [44–46]. T. T. Song et al.. investigated the effects of various parameters on complex dynamics in Spin-VCSELs under optical feedback [47]. R. Al-Seyab et al.. utilized the spin-flip model (SFM) and largest Lyapunov exponent (LLE) analysis to examine stable and unstable regions in Spin-VCSEL systems [48]. The nonlinear dynamics of Spin-VCSELs have also been successfully applied in high-speed photonic reservoir computing (RC) applications [49]. However, to the best of our knowledge, there have been no reported studies on the related dynamic behavior of PSNN neurons based on Spin-VCSEL. Compared with traditional VCSEL, optically pumped Spin-VCSEL has richer polarization dynamics, therefore, the parameters influence on neuron spiking are also different. In addition, the spiking delay can be flexibly adjusted over a larger range by pump ellipticity, which is significant for the design of PSNN towards complex tasks [32].

Based on the aforementioned considerations, this study proposes Spin-VCSEL as the neuron for PSNN and comprehensively discusses the excitatory and inhibitory spiking dynamics. Furthermore, the feasibility of spiking information propagation between two cascaded Spin-VCSEL neurons is analyzed. Our work is meaningful on enriching the polarization dynamics of Spin-VCSEL-based spiking neuron, and can provide valuable guideline for manipulation and optimization of this neuron.

The content of this paper is divided into three parts: Firstly, the structure and theoretical model of Spin-VCSEL are presented. This section provides a detailed description of the Spin-VCSEL's architecture and establishes a theoretical model to analyze its behavior. Secondly, the influence and physical mechanism of external disturbances on the dynamics of Spin-VCSEL are discussed. Various factors that affect the performance of Spin-VCSELs are examined, and their underlying physical mechanisms are explored. Finally, high-quality spiking propagation in cascaded Spin-VCSELs is demonstrated. The ability of two cascaded Spin-VCSEL neurons to propagate spiking information effectively is investigated and showcased. This analysis focuses on understanding how spiking information can be effectively transmitted from one neuron to another within a network configuration of PSNN. By addressing these aspects, this study aims to contribute to a better understanding of using Spin-VCSEL as a neuron in PSNN systems.

2 Theoretical model

Figure 1 illustrates the schematic diagram of the neuron used in the photonic spiking neural network (PSNN), which consists of cascaded, optically pumped Spin-VCSELs. The output of a semiconductor laser (SL) is externally modulated using an electro-optical modulator (EOM) driven by a signal generator (SG). This modulated output is then injected into a Spin-VCSEL, i.e., transmitter (T-Spin-VCSEL) through a circulator (CIR1). By controlling external perturbation intensity and other parameters, the spiking output and LIF function can be achieved based on the switching from injection locking to partial locking. To study spike propagation characteristics between cascaded neurons, the T-Spin-VCSEL output is divided into two paths using an optical coupler (OC). One path is detected by a polarization beam splitter (PBS2) and photodetectors (PD3 and PD4). The other path is injected into another Spin-VCSEL, i.e., receiver (R-Spin-VCSEL) via CIR2 and detected using PBS1 and photodetectors (PD1 and PD2). The nonlinear dynamics for cascaded Spin-VCSELs can be described based on the spin-flip model (SFM), as discussed in previous studies [45, 47, 49]:

$$\frac{dE_{+,T}}{dt} = k\left(N_T + n_T - 1\right)\left(1 + i\alpha\right)E_{+,T} - \left(\gamma_a + i\gamma_p\right)E_{-,T} + k_{inj+,T}\left[E_{inj} + \Delta E\left(t\right)\right]e^{i\Delta\omega_1 t} + F_{+,T} \tag{1}$$

$$\frac{dE_{-,T}}{dt} = k\left(N_T - n_T - 1\right)\left(1 + i\alpha\right)E_{-,T} - \left(\gamma_a + i\gamma_p\right)E_{+,T} + k_{inj-,T}\left[E_{inj} + \Delta E\left(t\right)\right]e^{i\Delta\omega_1 t} + F_{-,T} \tag{2}$$

$$\frac{dE_{\pm,R}}{dt} = k\left(N_R \pm n_R - 1\right)\left(1 + i\alpha\right)E_{\pm,R} - \left(\gamma_a + i\gamma_p\right)E_{\mp,R} + k_{inj,R}E_{\pm,T}(t-\tau)e^{i\Delta\omega_2 t - i\omega_T\tau} + F_{\pm,R} \tag{3}$$

$$\frac{dN_{T,R}}{dt} = \gamma_N\left[\,\eta_{T,R} - \left(1 + \left|E_{+,T,R}\right|^2 + \left|E_{-,T,R}\right|^2\right) N_{T,R} - n_{T,R}\left(\left|E_{+,T,R}\right|^2 - \left|E_{-,T,R}\right|^2\right)\,\right] \tag{4}$$

$$\frac{dn_{T,R}}{dt} = \gamma_N P_{T,R}\eta_{T,R} - \left[\gamma_S + \gamma_N\left(\left|E_{+,T,R}\right|^2 + \left|E_{-,T,R}\right|^2\right)\right] n_{T,R} - \gamma_N\left(\left|E_{+,T,R}\right|^2 - \left|E_{-,T,R}\right|^2\right) N_{T,R} \tag{5}$$

$$F_{\pm,T,R} = \xi_{a,b}\sqrt{\beta_{T,R}\gamma_N\left(N_{T,R} \pm n_{T,R}\right)} \tag{6}$$

Here, Eq. (1) describes the dynamics of cascaded Spin-VCSELs, T and R represent the T-Spin-VCSEL and R-Spin-VCSEL, respectively. E_+ and E_- are the slowly varying amplitudes of the optical fields for RCP and LCP, respectively. The third term on the right side of Eq. (1) represents optical injection, with E_{inj} representing the continuous injection amplitude and ΔE representing external disturbance. $N_{\mathrm{T,\,R}}$ is the total carrier population inversion, while $n_{\mathrm{T,\,R}}$ accounts for the difference between carrier inversions for spin-up and spin-down channels. $P_{\mathrm{T,\,R}}$ denotes pump ellipticity of transmitter and receiver. $\Delta\omega_1$ and $\Delta\omega_2$ (where $\Delta\omega_1 = \omega_{\mathrm{inj}}$ - ω_{T} and $\Delta\omega_2 = \omega_{\mathrm{T}}$ - ω_{R}) represent angular frequency detuning of optical injection relative to free-running condition. Here, ω_{inj}, ω_{T}, ω_{R} correspond to angular frequencies of external injection signal, T-Spin-VCSEL output and R-Spin-VCSEL output respectively. $F_{+,\mathrm{T,\,R}}$, $F_{-,\mathrm{T,\,R}}$ are the noise terms. $\xi_{\mathrm{a,\,b}}$ represents independent Gaussian white noise with unit variance and zero mean values. In addition, $k_{\mathrm{inj+,T}}$ and $k_{\mathrm{inj-,T}}$ are the injection strengths of T-Spin-VCSEL for the component of RCP and LCP respectively, $k_{\mathrm{inj,\,R}}$ is the injection strength from transmitter to receiver. For simplicity, within this study, it is assumed that both Spin-VCSELs have identical physical parameters such as k, α, γ_{a}, γ_{p}, $\beta_{\mathrm{T,\,R}}$,γ_{N}, γ_{s}, and $\eta_{\mathrm{T,\,R}}$. In our simulation, for RCP

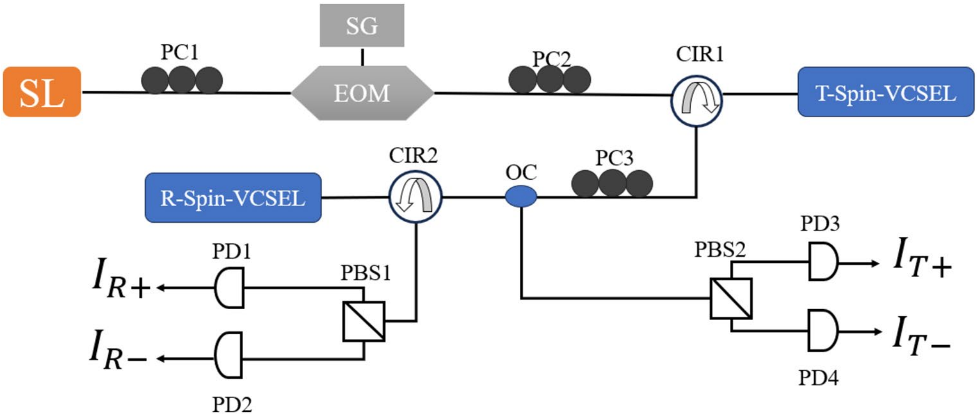

Fig. 1 Schematic diagram of PSNN neuron based on optically pumped Spin-VCSEL. SL: Semiconductor laser; EOM: Electro-optic modulator; PC: Polarization controller; T-Spin-VCSEL: Transmitter of Spin-VCSEL; R-Spin-VCSEL: Receiver of Spin-VCSEL; SG: Signal generator; CIR: Circulator; PBS: Polarization beam splitter; PD: Photodetector; OC: optical coupler

Table 1 Physical parameters used in simulation

Parameters	Description	Value
k	Decay rate of optical field	250 ns^{-1}
γ_a	Rate of linear dichroism	2 ns^{-1}
γ_p	Rate of birefringence	10 ns^{-1}
γ_N	Decay rate of N	1 ns^{-1}
γ_s	Spin-flip rate	100 ns^{-1}
$\eta_{T,R}$	Pump intensity of transmitter and receiver	2
E_{inj}	Injection amplitude of continuous component	0.5
$\beta_{T,R}$	Spontaneous emission factor	10^{-6}
τ	Time-delay from transmitter to receiver	10 ns
α	Linewidth enhancement factor	2.2

optical injection, $k_{inj+,T}$ =125 ns^{-1}, $k_{inj-,T} = 0$ ns^{-1}; for LCP optical injection, $k_{inj+,T} = 0$ ns^{-1}, $k_{inj-,T} = 125$ ns^{-1}. The used physical parameters are listed in Table 1 unless otherwise specified.

3 Results and discussions

3.1 Excitatory spiking dynamics of Spin-VCSEL

Firstly, we investigate the output intensity and ellipticity as functions of η_T and P_T under free-running condition, the results are shown in Fig. 2(a) and (b), where $P_T = 1$ in (a) and $\eta_T = 2$ in (b). Here, $I_{T,\pm} = |E_{T,\pm}|^2$, the output ellipticity P_{out} is defined as $(I_{T,+} - I_{T,-})/(I_{T,+} + I_{T,-})$. From (a), the output intensity of RCP is significantly larger than LCP as a result of RCP pump. The physical mechanism is associated with the unbalanced number of spin-polarized carriers, represented by $N_T + n_T$ and $N_T - n_T$, which can be controlled by P_T. From (b), we can obtain the opposite P_{out} under the pump ellipticity P_T and $-P_T$. Furthermore, under $P_T = 0$, the same free-running output ($I_{T,+} = I_{T,-} = 0.508$) can be found. Note that the unique polarization manipulation capability using spin-VCSEL agrees well with that of experimental report in Ref [37]. , confirming the reliability of our numerical simulation.

We then exploit the excitatory spiking dynamics under RCP optical injection. The results under LCP optical injection will be demonstrated latter. Figure 3(a1)-(f1) show the normalized intensity of RCP and LCP ($I_{T,\pm}$) of T-Spin-VCSEL varies with the change of ΔE, where $\Delta f_1 = \Delta\omega_1/2\pi$

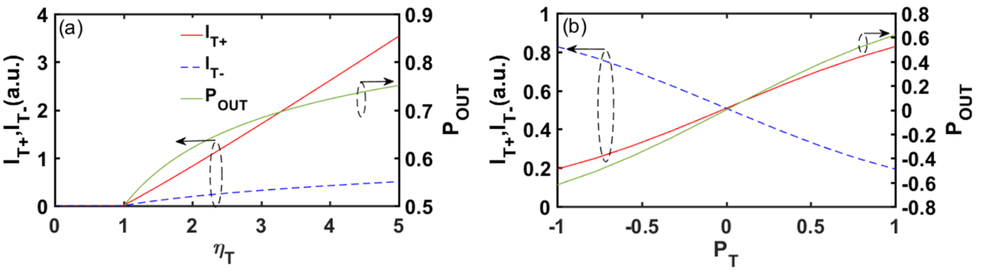

Fig. 2 Under free-running condition, normalized intensity ($I_{T,\pm}$) of RCP (red), LCP (blue), and the output ellipticity (P_{out}, green) as functions of η_T (**a**) and P_T (**b**). In (**a**), $P_T = 1$. In (**b**), $\eta_T = 2$

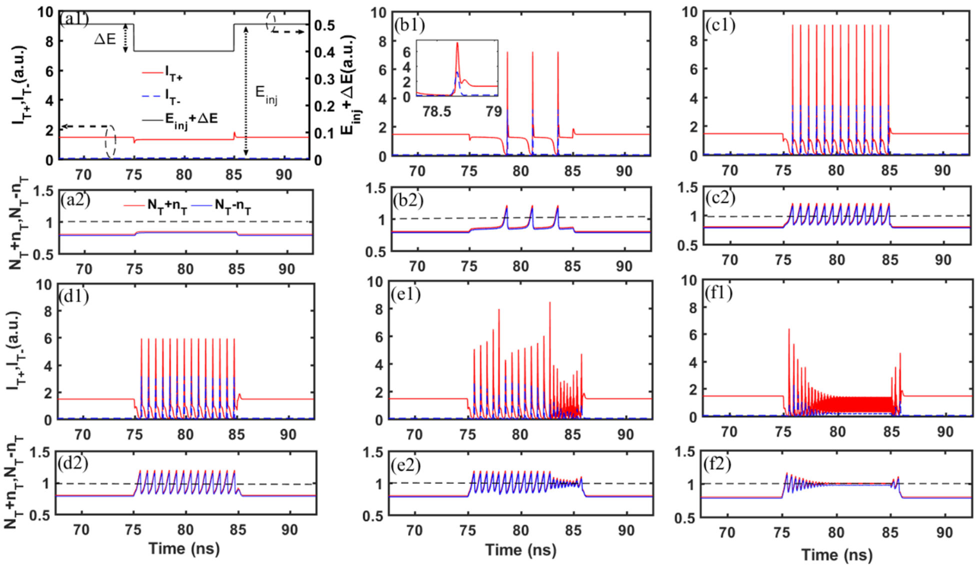

Fig. 3 (**a1**–**f1**) Normalized intensity ($I_{T,\pm}$) of RCP (red) and LCP (blue) varies with ΔE; (**a2**–**f2**) Corresponding spin-polarized carriers $N_T + n_T$ and $N_T - n_T$. $\Delta f_1 = -16$ GHz, $P_T = 1$, $f_p = 40$ MHz, $T_d = 10$ ns, $k_{inj+,T} = 125$ ns^{-1}, $k_{inj-,T} = 0$ ns^{-1}. In (a1)-(f1) and corresponding (**a2**–**f2**), ΔE is -0.1, -0.107, -0.14, -0.18, -0.195, and -0.25 respectively

= -16 GHz, $P_T = 1$, $k_{inj+,T} = 125\ ns^{-1}$, $k_{inj-,T} = 0\ ns^{-1}$. The frequency of stimulus spiking (f_p) and duration (T_d) are 40 MHz and 10 ns respectively. In (a1)-(f1), the value of ΔE is -0.1, -0.107, -0.14, -0.18, -0.195 and − 0.25, respectively. The corresponding spin-polarized carriers $N_T + n_T$ and N_T - n_T are shown in (a2)-(f2). In Fig. 3(a1), it can be observed that, for smaller values of |ΔE|, a larger continuous injection component ($k_{inj}E_{inj}$) leads to injection locking of RCP to the external signal in T-Spin-VCSEL, resulting in a stable output of RCP while the output intensity of LCP is close to 0. Note that the overshoot and undershoot can be seen at the edges of negative stimulus due to the abrupt variation of $N_T + n_T$ and N_T - n_T [see (a2)]. Figure 3(b1) shows that when the external disturbance ΔE reaches − 0.107, both RCP and LCP modes of T-Spin-VCSEL simultaneously emit sub-nanosecond spikes. Upon removal of the disturbance, the laser output returns to an injection locked state. This behavior is similar to LIF characteristics observed in biological neurons [7]. The firing of RCP(LCP) occurs whenever the corresponding $N_T + n_T$ (N_T - n_T) is recovered (due to negative stimulus) and exceeds the threshold 1, see (b2). Once a spike is generated, the carrier depletion makes the output intensity enter a refractory period. Figure 3(c1-d1) demonstrate that when ΔE is set at -0.14 and − 0.18, the two polarization modes of T-Spin-VCSEL exhibit high-frequency tonic spiking output. However, for ΔE = -0.195 shown in (e1), the quasi-periodic state is generated in both polarization modes. Furthermore, Fig. 3(f1) illustrates that for ΔE = -0.25, the output enters a RO state.

Figure 4 show the bifurcation diagrams of maximal output intensity as a function of ΔE under P_T = 1. Here, the outputs of RCP and LCP are demonstrated in left column (a1-e1) and right column (a2-e2) respectively. The range shown here is limited to ΔE ∈ [-0.3, 0], as outputs enter RO

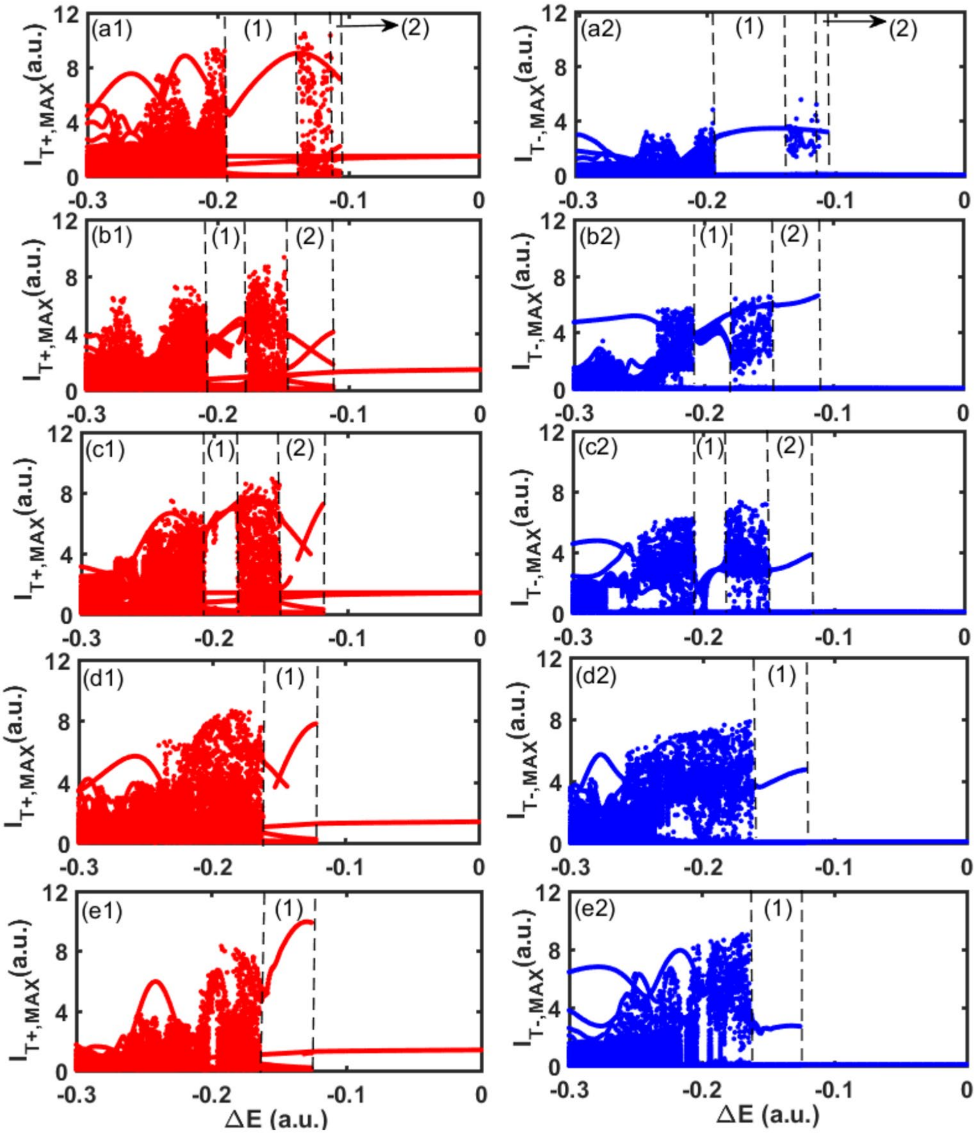

Fig. 4 Bifurcation diagrams of maximal output intensity as a function of ΔE under different pump ellipticity P_T. (**a1**, **a2**): P_T = 1; (**b1**, **b2**): P_T = 0.5; (**c1**, **c2**): P_T = 0; (**d1**, **d2**): P_T= -0.5; (**e1**, **e2**): P_T = -1. f_p = 40 MHz, Δf_1 = -16 GHz, T_d = 10 ns, $k_{inj+,T}$ = 125 ns^{-1}, $k_{inj-,T}$ = 0 ns^{-1}. Regions (1) and (2) correspond to tonic spiking. Left column: RCP outputs; Right column: LCP outputs

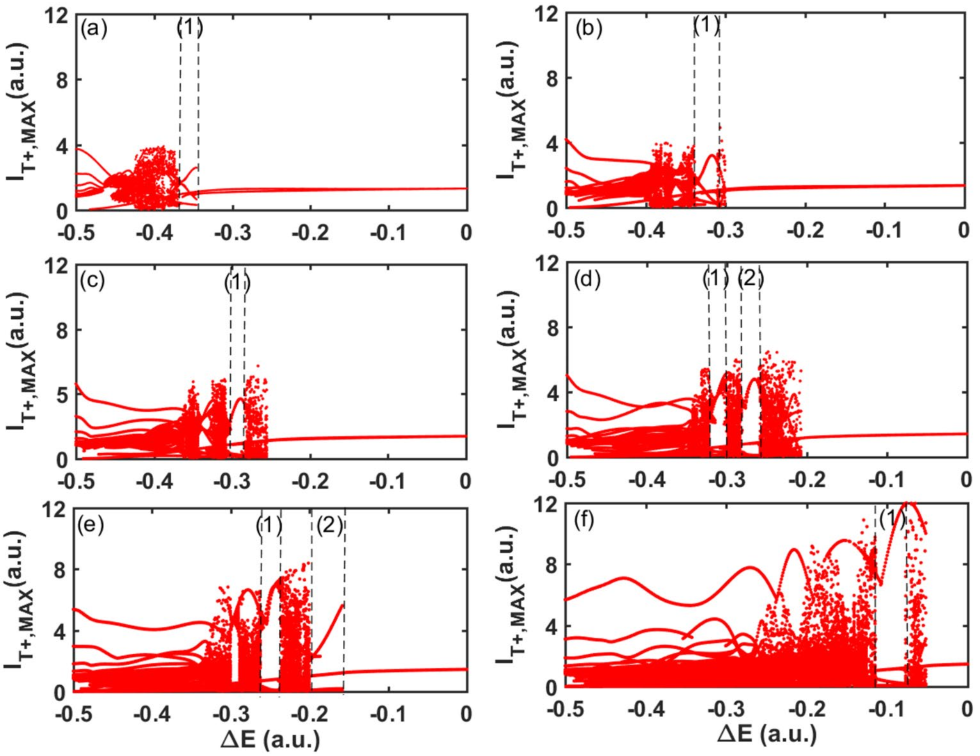

Fig. 5 Bifurcation diagram of RCP as a function of ΔE under different injection detuning Δf_1. (**a**): Δf_1 = -6 GHz; (**b**): Δf_1 = -8 GHz; (**c**): Δf_1 = -10 GHz; (**d**): Δf_1 = -12 GHz; (**e**): Δf_1 = -14 GHz; (**f**): Δf_1 = -18 GHz. f_p = 40 MHz, P_T = 1, T_d = 10 ns, $k_{inj+,T}$ = 125 ns^{-1}, $k_{inj-,T}$ = 0 ns^{-1}. Regions (1) and (2) correspond to tonic spiking

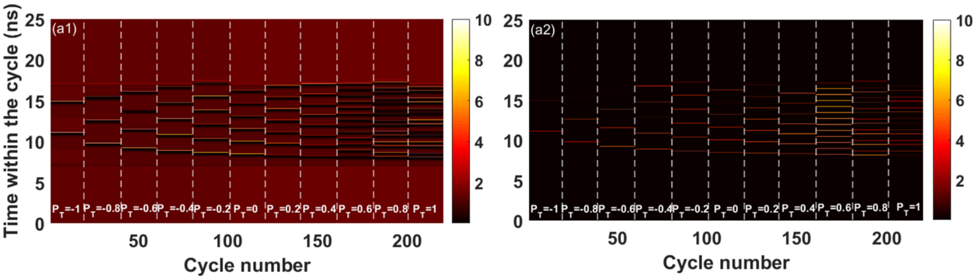

Fig. 6 Temporal maps plotting of the output response for RCP (**a1**) and LCP (**a2**) under different pump ellipticity P_T. ΔE = -0.126, Δf_1 = -16 GHz, f_p = 40 MHz, T_d = 10 ns, $k_{inj+,T}$ = 125 ns^{-1}, $k_{inj-,T}$ = 0 ns^{-1}

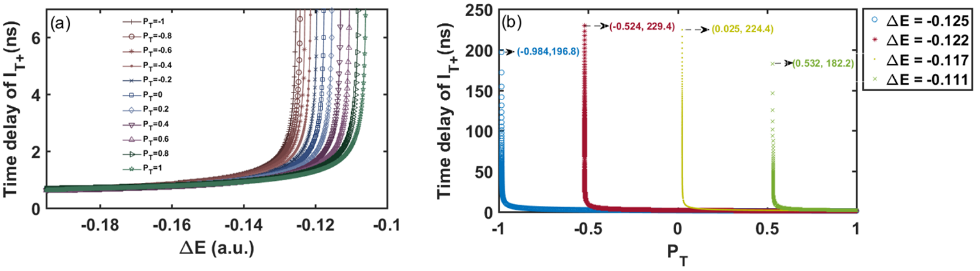

Fig. 7 (**a**) Under different pump ellipticity P_T, spiking delay of RCP varies with ΔE; (**b**) Variation of spiking delay for RCP as a function of P_T under the different ΔE. Δf_1 = -16 GHz, f_p = 40 MHz, T_d = 10 ns, $k_{inj+,T}$ = 125 ns^{-1}, $k_{inj-,T}$ = 0 ns^{-1}

and chaos states for the range of $\Delta E \in$ [-0.5, -0.3]. The bifurcation diagram reveals various regions: (1) and (2) regions where tonic spiking occurs; other regions corresponding to stable output, RO or chaos state. These results demonstrate that coexistence between the two polarization modes is possible within certain ranges of ΔE values and complex nonlinear dynamics such as periodic and chaotic states can be observed. The region of generating spiking pulse are similar for both RCP/LCP, as seen from the comparison of Fig. 4(a1)-(e1) and (a2)-(e2). We observed that for various pump ellipticity P_T, the different polarization dynamics can be obtained, therefore, the generation region of ΔE for tonic spiking should be varied accordingly.

Figure 5 presents the bifurcation diagram of RCP with external disturbance ΔE under different injection detuning Δf_1, where P_T = 1, f_p = 40 MHz, T_d = 10 ns, $k_{inj+,T}$ = 125 ns^{-1}, and $k_{inj-,T}$ = 0 ns^{-1}. To ensure that the system remains in an injection locked state without any disturbance, negative detuning values are selected. It can be observed that when Δf_1 is -12 and $-$14 GHz, two tonic spiking regions

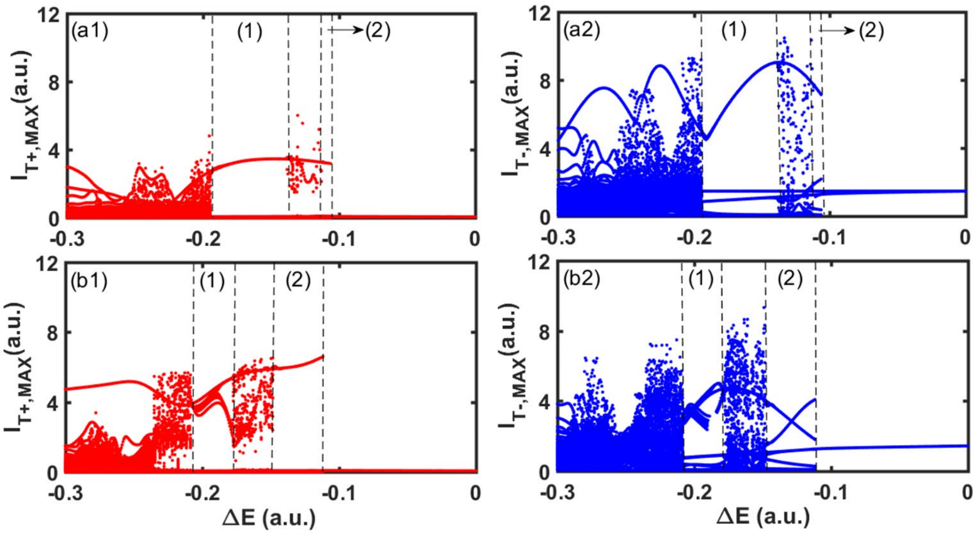

Fig. 8 Bifurcation diagram of RCP (left column) and LCP (right column) outputs as a function of ΔE under LCP optical injection. (**a1**, **a2**): P_T = -1; (**b1**, **b2**) P_T = -0.5. f_p = 40 MHz, Δf_1 = -16 GHz, T_d = 10 ns, $k_{inj+,T}$ = 0 ns^{-1}, $k_{inj-,T}$ = 125 ns^{-1}

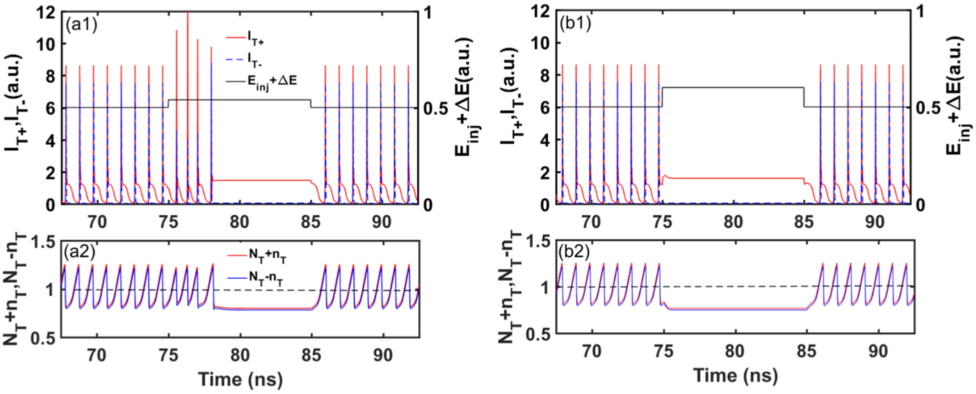

Fig. 9 (**a1**, **b1**) Inhibitory spiking dynamics behavior of RCP (red) and LCP (blue) output under different ΔE. (**a2**, **b2**) Corresponding spin-polarized carriers $N_T + n_T$ and N_T - n_T. (**a1**, **a2**): ΔE=0.04, (**b1**, **b2**): ΔE=0.1. Δf_1 = -21 GHz, f_p = 40 MHz, T_d = 10 ns, P_T = 1, $k_{inj+,T}$ = 125 ns^{-1}, $k_{inj-,T}$ = 0 ns^{-1}

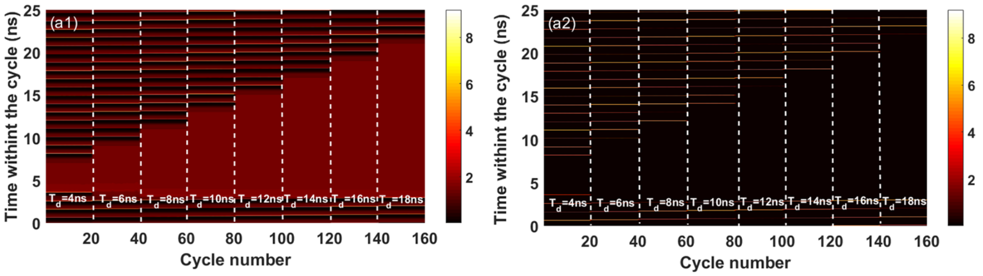

Fig. 10 Temporal maps plotting of inhibitory output for RCP (**a1**) and LCP (**a2**) under different T_d. Δf_1 = -21 GHz, f_p = 40 MHz, P_T = 1, ΔE=0.1, $k_{inj+,T}$ = 125 ns^{-1}, $k_{inj-,T}$ = 0 ns^{-1}

exist [see (d), (e)]. When Δf_1 is -6, -8, -10 and -18 GHz, only region (1) generates tonic spiking while the rest exhibit RO or chaotic states [see (a)-(c), and (f)]. Although not shown here, as $|\Delta f_1|$ decreases further, the region generating tonic spiking almost disappears. Furthermore, as $|\Delta f_1|$ decreases, a larger threshold of $|\Delta E|$ is required to transition from injection locking to partial locking. Therefore, selecting appropriate values for both Δf_1 and ΔE is crucial for achieving ideal spiking behavior.

Figure 6 displays temporal maps of output response for RCP (a) and LCP (b) under different pump ellipticity value P_T. The parameters used are f_p = 40 MHz, ΔE = -0.126, Δf_1 = -16 GHz, T_d = 10 ns, $k_{inj+,T}$ = 125 ns^{-1}, $k_{inj-,T}$ = 0 ns^{-1}. The results demonstrate that as P_T increases, the tonic spiking generated by both RCP and LCP modes becomes more frequent or dense. This indicates that compared to traditional VCSEL spiking neurons [15–24], the proposed neuron utilizing Spin-VCSEL offers a new dimension for manipulation. Furthermore, with an increase in P_T, the spiking delay between the first occurrence of a spike and the start of external disturbance is reduced for both polarization modes.

Figure 7(a) illustrates the variation of spiking delay with ΔE under different pump ellipticity values P_T for RCP. Since the spiking delay for RCP is similar to that of LCP, only RCP is shown here. It should be noted that the repetition

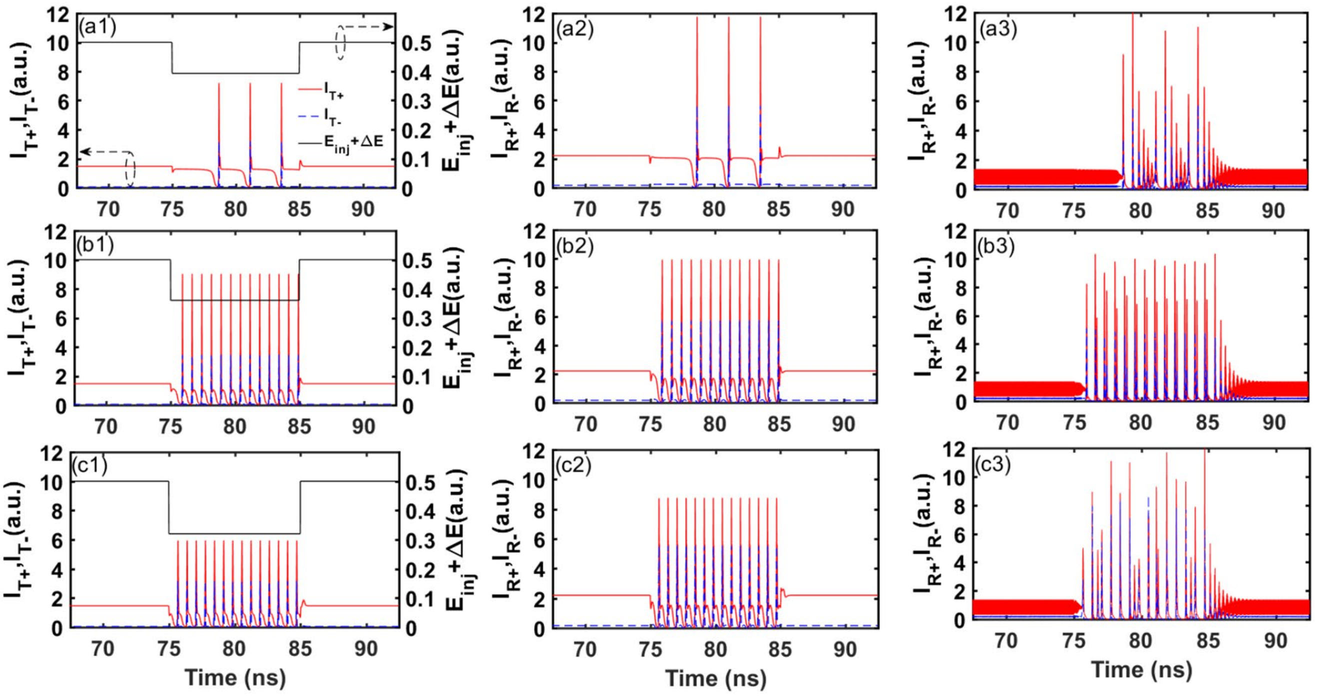

Fig. 11 Propagation characteristics of spikes generated by T-Spin-VCSEL (left column) and received by R-Spin-VCSEL (middle and right columns) for different Δ*E*. For T-Spin-VCSEL, (**a1**): Δ*E* = -0.107, (**b1**): Δ*E* = -0.14, (**c1**): Δ*E* = -0.18. For R-Spin-VCSEL, (**a2**–**c2**): $k_{\text{inj, R}}$ = 125 ns^{-1}. (**a3**–**c3**): $k_{\text{inj, R}}$ = 50 ns^{-1}. Δf_1 = -16 GHz, Δf_2 = -15.6 GHz, $P_{\text{T, R}}$ = 1, T_d = 10 ns, f_p = 40 MHz, $k_{\text{inj+,T}}$ = 125 ns^{-1}, $k_{\text{inj-,T}}$ = 0 ns^{-1}

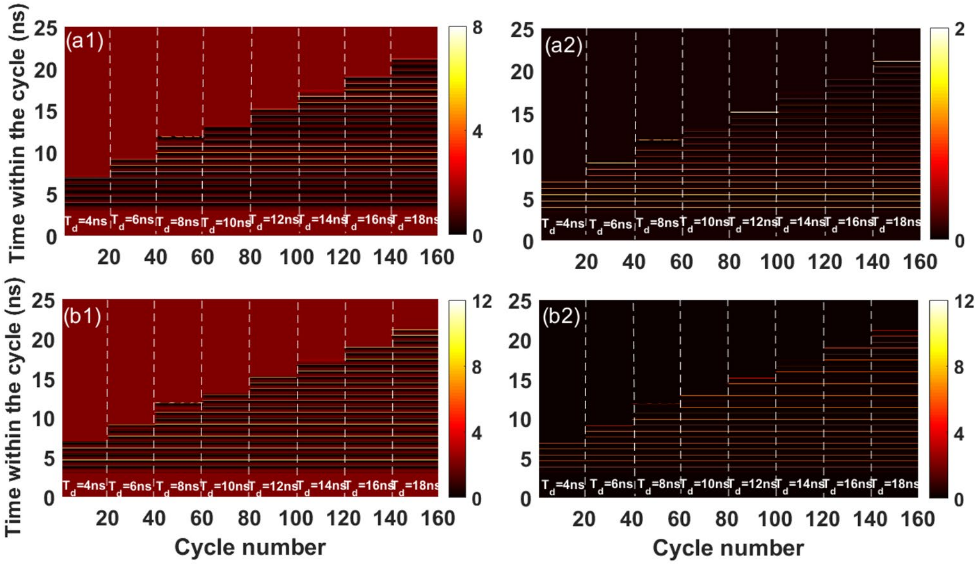

Fig. 12 Temporal maps plotting of spiking response for the two Spin-VCSELs with different T_d. Δ*E* = -0.14, the other parameters are the same as Fig. 11(**b1**) and (**b2**). (**a1**–**a2**) is the output of T-Spin-VCSEL, (**b1**–**b2**) is the output of R-Spin-VCSEL, the left and right columns correspond to RCP and LCP outputs respectively

period of the tonic spiking train is essentially close to the spiking delay defined above [22], and thus only the spiking delay is demonstrated in this figure. As depicted in Fig. 7(a), the spiking delay decreases as |Δ*E*| increases. This implies that when operating far from the locking region, higher frequency spiking can be generated. By careful simulations, we found that the maximal time-delay is always obtained when Δ*E* closes to the transition point from injection locking state to spiking state. For instance, under the given parameters of Fig. 4, these transition values of Δ*E* are − 0.125, -0.122, -0.117, and − 0.111 for P_T = -1, -0.5, 0, 0.5 respectively. To demonstrate the delay enhancement around these Δ*E* values, Fig. 7(b) shows the spiking delay as a function of P_T within the range [-1, 1]. It can be observed that, the larger time-delay can be achieved when P_T is -0.984, -0.524, 0.025, 0.532, thus confirming the above conclusion. As an example, for Δ*E* = -0.125 and P_T = -0.984, a time-delay as large as 196.8 ns can be obtained. Note that when

ΔE deviates from these optimization points, the time-delay adjustment range is typically within ~10 ns when changing P_T, as shown in Fig. 7(a). Therefore, by precisely adjusting system parameters, a wider range of delay adjustment can be achieved, thus providing a new control way for training photonic spiking neural networks (PSNN) based on delay-weight adjustment [27, 32]. This flexible and larger tunability range using Spin-VCSEL is particularly valuable when processing more complex tasks with fewer presynaptic neurons [32].

Although the excitatory spiking dynamics demonstrated above is under RCP optical injection, further study shows that, the spiking dynamics under LCP optical injection at the pump ellipticity P_T is the same with that of RCP optical injection at -P_T. As an example, Fig. 8 shows the bifurcation diagram of RCP and LCP outputs as a function of ΔE under LCP optical injection, where $P_T = -1$ [(a1, a2)] and $P_T = -0.5$ [(b1, b2)]. In this case, under free-running, the LCP output intensity is significantly larger than RCP component [see Fig. 2(b)]. Hence, this case belongs to parallel polarization optical injection (PPOI). By careful comparison, we found that the bifurcation of RCP(LCP) outputs [Fig. 8(a1, a2), $P_T = -1$] is basically the same with that of LCP(RCP) outputs shown in Fig. 4(a1) and (a2) ($P_T = 1$). Similarly, by comparing Fig. 8(b1, b2) ($P_T = -0.5$) and Fig. 4(b1, b2) ($P_T = 0.5$), the same symmetry can also be obtained. Hence, due to the symmetry pointed above, in the following, we will discuss the inhibitory spiking dynamics only under RCP optical injection.

3.2 Inhibitory spiking dynamics of Spin-VCSEL

We also explored the inhibitory spiking dynamics of photonic neurons using positive external disturbance ($\Delta E > 0$) for Spin-VCSEL. Figure 9 shows the inhibitory spiking dynamics behavior of RCP (red) and LCP (blue) output under different ΔE, where Δf_1 = -21 GHz, f_p = 40 MHz, T_d = 10 ns, P_T = 1, $k_{inj+,T}$ = 125 ns^{-1}, $k_{inj-,T}$ = 0 ns^{-1}. In Fig. 9(a1), the system parameters were carefully adjusted to ensure that both RCP and LCP modes exhibit tonic spiking in the absence of any external stimulus. However, when a weak external stimulus with $\Delta E = 0.04$ is applied, the number of spikes in both modes is reduced during the stimulation duration, but tonic spiking still persists. When ΔE is increased to 0.1, as shown in Fig. 9(b1), both of spiking for RCP and LCP modes are completely suppressed, successfully emulating inhibitory dynamics seen in biological neurons [19]. The physical mechanism is attributed to the carrier depletion due to the positive stimulus, as shown in Fig. 9(a2) and (b2). Figure 10 presents the output state diagram of both modes under different T_d values while keeping ΔE fixed at 0.1 and other parameters unchanged from Fig. 9. It can be observed that with these given parameters, varying T_d leads to effective suppression of tonic spiking in LCP and RCP modes. Furthermore, the dynamic behaviors of the two modes demonstrate good consistency within this range of parameter variations.

3.3 Spiking propagation characteristics of cascaded Spin-VCSELs

In this section, we will discuss the effects of stimulus perturbation ΔE and duration T_d on the spiking propagation characteristics between two cascaded neurons. Figure 11 illustrates the spikes generated by T-Spin-VCSEL and received by R-Spin-VCSEL under different ΔE values. The parameters used are $P_{T,R}$ = 1, T_d = 10 ns, Δf_1 = -16 GHz, $k_{inj+,T}$ = 125 ns^{-1}, $k_{inj-,T}$ = 0 ns^{-1}, and $\Delta f_2 = \Delta\omega_2/2\pi$ = -15.6 GHz. It is assumed that the polarization modes of the transmitter are injected into the same mode at the receiver. For ease of comparison, the laser output at the receiver is shifted forward by a delay of τ (i.e., 10 ns) during plotting. For a perturbation of ΔE = -0.107 [see (a1)], the polarization modes of T-Spin-VCSEL can generate three spikes. When these spikes propagate to R-Spin-VCSEL, both of LCP and RCP modes also produce similar spikes with the same number for a proper injection strength $k_{inj,R}$ = 125 ns^{-1}[see (a2)]. However, for a lower injection strength, quasi-periodic pulse would be produced at the receiver, as shown in Fig. 11(a3), where $k_{inj,R}$ = 50 ns^{-1}. By increasing the intensity of disturbance to ΔE = -0.14 and ΔE = -0.18 [see (b1)-(b3), (c1)-(c3)], we can observe similar responses.

Figure 12(a) and (b) depict state diagrams of spiking responses for the two Spin-VCSELs under different T_d values, where ΔE is fixed at -0.14 and other parameters are identical to those in Fig. 11(b1) and (b2). By adjusting the duration of the disturbance, T-Spin-VCSEL can achieve controllable spiking response times, which can then propagate successfully to R-Spin-VCSEL, reproducing similar spikes with the same number. Further investigation reveals that for unidirectionally-coupled Spin-VCSEL neurons, only under strong enough injection strength stimulation can the receiver generate a spiking response. This conclusion is supported by Fig. 13(a1) and (a2), which presents a bifurcation diagram of R-Spin-VCSEL as a function of $k_{inj,R}$. From this figure, it can be inferred that tonic spiking generation occurs when $k_{inj,R} > \sim 90$ ns^{-1}. The threshold feature is similar to conventional electric pumping VCSEL [50], for which a successful and high-quality spiking propagation can be realized when the coupling strength exceeds a certain value. We also simulated the bifurcation diagram of R-Spin-VCSEL under various detuning Δf_2 and pump ellipticity P_R of R-Spin-VCSEL. The results are shown in Fig. 13(b1), (b2), (c1) and (c2). It is observed that the spiking patterns

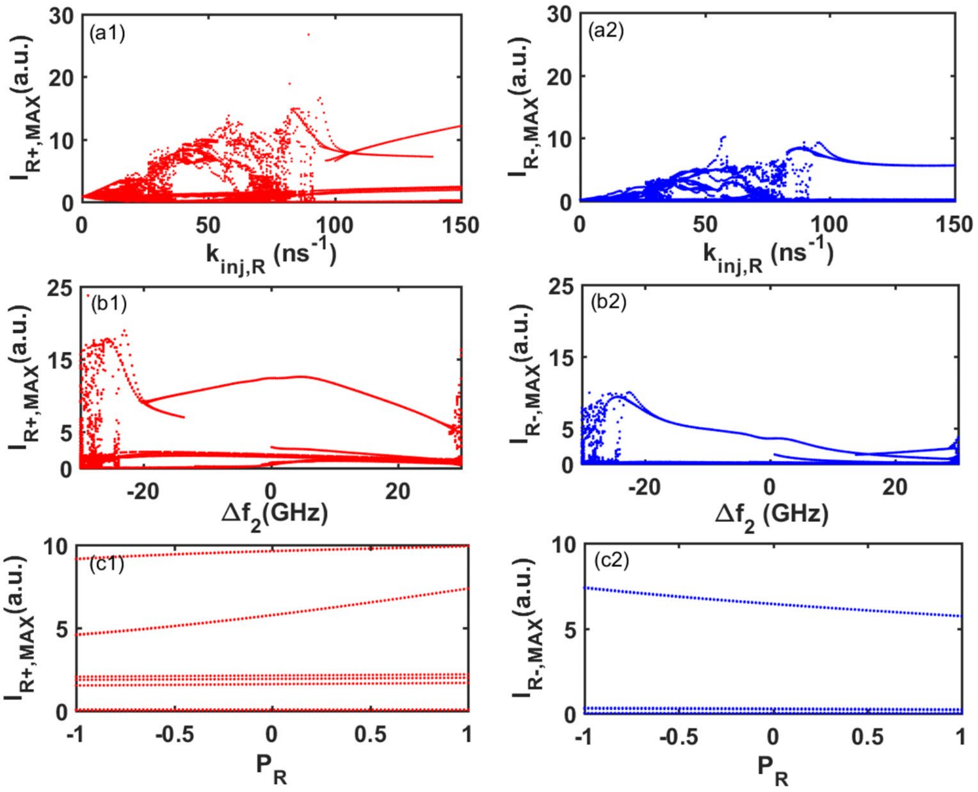

Fig. 13 Bifurcation diagram of R-Spin-VCSEL as functions of $k_{inj,R}$ [(**a1**), (**a2**)], Δf_2 [(**b1**), (**b2**)], and P_R [(**c1**), (**c2**)]. For T-Spin-VCSEL, ΔE = -0.14, P_T = 1, T_d = 10 ns, f_p = 40 MHz, Δf_1 = -16 GHz, $k_{inj+,T}$ = 125 ns^{-1}, $k_{inj-,T}$ = 0 ns^{-1}. For R-Spin-VCSEL, (**a1**), (**a2**): Δf_2 = -15.6 GHz, P_R = 1; (**b1**), (**b2**): $k_{inj,R}$ = 125 ns^{-1}, P_R = 1; (**c1**), (**c2**): $k_{inj,R}$ = 125 ns^{-1}, Δf_2 = -15.6 GHz. The left and right columns correspond to RCP and LCP outputs respectively

can be propagated successfully over a wide optimization range of Δf_2 (within the range of -23.5 ~ 29 GHz under P_R = 1). Furthermore, the spiking propagation is not sensitive to the value of P_R under the detuning Δf_2 = -15.6 GHz.

4 Conclusions

In summary, the excitability and inhibitory spiking dynamics of Spin-VCSEL neurons have been explored theoretically. We also investigated the propagation behavior of spike information between two unidirectionally-coupled Spin-VCSEL neurons. The results are summarized as follows: (1) Controllable and repeatable spiking modes can be achieved using negative stimulation and adjusting the parameters such as external disturbance intensity, pump ellipticity, and injection detuning. (2) Considering the various possibilities in neuron output, including tonic spiking, phasic spiking, steady state, RO, chaos, etc., it is important to select the reasonable range of parameters. (3) Under certain conditions with positive stimulation, inhibitory spiking dynamics can be achieved. (4) The spiking signal generated by T-Spin-VCSEL can be successfully propagated to R-Spin-VCSEL with identical spike numbers and time intervals when the injection strength of receiver is larger than a certain value. Compared with traditional VCSEL neurons, the advantages of Spin-VCSEL neurons include the superior polarization controlling capability [35–37], and more manipulation dimensions (such as pump ellipticity) to obtain the tunable spiking delay and interval over a large range, which is useful in designing the delay-weight PSNN towards complex tasks processing [27, 32]. On the other hand, a disadvantage of Spin-VCSEL is that it's more sensitive to external optical feedback, i.e., a smaller feedback strength may induce the chaos [47], which should be avoided in practical application. Our proposal can provide a new choice and "building block" for photonic spiking neuron; The related numerical analysis is meaningful on enriching the scientific cognition of polarization dynamics of Spin-VCSEL-based spiking neuron, and can provide valuable guideline for the manipulation of this neuron. Future work will be focused on the training method and applications for PSNN composed of Spin-VCSELs.

Author contributions Mei-Ling Zou conducted the modeling and simulation and wrote the manuscript. Xin-Hong Jia fully supervised the research and revised the manuscript. All authors conducted investigation and reviewed the manuscript.

Funding This work was supported by Sichuan Science and Technology Program (2024NSFSC0461); National Natural Science Foundation of China (NSFC) Nos. 61205079, 61901289; College Student Innovation Project of Sichuan Normal University in 2024 (X202410636193).

Data availability No datasets were generated or analysed during the current study.

Declarations

Competing interests The authors declare no competing interests.

Conflict of interest The authors declare that they have no known competing financial interests or personal relationships that could have appeared to influence the work reported in this paper.

References

1. B.J. Shastri, A.N. Tait, T. Ferreira de Lima, W.H.P. Pernice, H. Bhaskaran, C.D. Wright, P.R. Prucnal, Photonics for artificial intelligence and neuromorphic computing. Nat. Photonics. **15**, 102–114 (2021)
2. V. Bangari, B.A. Marquez, H.B. Miller, A.N. Tait, Digital electronics and analog photonics for convolutional neural networks (DEAP-CNNs). IEEE J. Sel. Top. Quantum Electron. **26**, 7701213 (2020)
3. A.N. Tait, M.A. Nahmias, B.J. Shastri, P.R. Prucnal, Broadcast and weight: an integrated network for scalable photonic spike processing. J. Lightwave Technol. **32**(21), 4029–4041 (2014)
4. J. Feldmann, N. Youngblood, C.D. Wright, H. Bhaskaran, W.H.P. Pernice, All-optical spiking neurosynaptic networks with self-learning capabilities. Nature. **569**, 208–214 (2019)
5. B.J. Shastri, M.A. Nahmias, A.N. Tait, P.R. Prucnal, Simulations of a graphene excitable laser for spike processing. Opt. Quant. Electron. **46**, 1353–1358 (2014)
6. K. Alexander, T.V. Vaerenbergh, M. Fiers, P. Mechet, J. Dambre, P. Bienstman, Excitability in optically injected microdisk lasers with phase controlled excitatory and inhibitory response. Opt. Express. **21**(22), 26182–26191 (2013)
7. M.A. Nahmias, B.J. Shastri, A.N. Tait, P.R. Prucnal, A leaky integrate-and-fire laser neuron for ultrafast cognitive computing. IEEE J. Sel. Top. Quantum Electron. **19**(5), 1800212 (2013)
8. G. Sarantoglou, M. Skontranis, A. Bogris, C. Mesaritakis, Experimental study of neuromorphic node based on a multiwaveband emitting two-section quantum dot laser. Photonics Res. **9**(4), B87–B95 (2021)
9. J.L. Xiang, A. Torchy, X.H. Guo, Y.K. Su, All-optical spiking neuron based on passive microresonator. J. Lightwave Technol. **38**, 4019–4029 (2020)
10. T. Van Vaerenbergh, M. Fiers, P. Mechet, T. Spuesens, R. Kumar, G. Morthier, B. Schrauwen, J. Dambre, P. Bienstman, Cascadable excitability in microrings. Opt. Express. **20**(18), 20292–20308 (2012)
11. J.L. Xiang, Y. Zhang, Y. Zhao, X.H. Guo, Y.K. Su, All-optical silicon microring spiking neuron. Photonics Res. **10**(4), 939–946 (2022)
12. F. Selmi, R. Braive, G. Beaudoin, I. Sagnes, R. Kuszelewicz, S. Barbay, Temporal summation in a neuromimetic micropillar laser. Opt. Lett. **40**(23), 5690–5693 (2015)
13. D. Rosenbluth, K. Kravtsov, M.P. Fok, P.R. Prucnal, A high performance photonic pulse processing device. Opt. Express. **17**(25), 22767–22772 (2009)
14. K. Kravtsov, M.P. Fok, D. Rosenbluth, P.R. Prucnal, Ultrafast all-optical implementation of a leaky integrate-and-fire neuron. Opt. Express. **19**, 2133–2147 (2011)
15. A. Hurtado, K. Schires, I.D. Henning, M.J. Adams, Investigation of vertical cavity surface emitting laser dynamics for neuromorphic photonic systems. Appl. Phys. Lett. **100**, 103703 (2012)
16. S.Y. Xiang, A.J. Wen, W. Pan, Emulation of spiking response and spiking frequency property in VCSEL- based photonic neuron. IEEE Photon J. **8**(5), 1504109 (2016)
17. S.Y. Xiang, Y.H. Zhang, X.X. Guo, A.J. Wen, Y. Hao, Photonic generation of neuron-like dynamics using VCSELs subject to double polarized optical injection. J. Lightw Technol. **36**(19), 4227–4234 (2018)
18. A. Hurtado, J. Javaloyes, Controllable spiking patterns in long-wavelength vertical cavity surface emitting lasers for neuromorphic photonics systems. Appl. Phys. Lett. **107**(24), 1103 (2015)
19. J. Robertson, T. Deng, J. Javaloyes, A. Hurtado, Controlled inhibition of spiking dynamics in VCSELs for neuromorphic photonics: theory and experiments. Opt. Lett. **42**(8), 1560–1563 (2017)
20. T. Deng, J. Robertson, A. Hurtado, Controlled propagation of spiking dynamics in vertical-cavity surface-emitting lasers: towards neuromorphic photonic networks. IEEE J. Sel. Top. Quantum Electron. **23**(6), 1800408 (2017)
21. T. Deng, J. Robertson, Z.M. Wu, G.Q. Xia, X.D. Lin, X. Tang, Z.J. Wang, A. Hurtado, Stable propagation of inhibited spiking dynamics in vertical-cavity surface-emitting lasers for neuromorphic photonic networks. IEEE Access. **6**, 67951–67958 (2018)
22. Y. Lu, W. Zhang, B.Q. Fu, Z.Y. He, Frequency-switched photonic spiking neurons. Opt. Express. **30**, 21599–21608 (2022)
23. S. Barbay, R. Kuszelewicz, A.M. Yacomotti, Excitability in a semiconductor laser with saturable absorber. Opt. Lett. **36**, 4476–4478 (2011)
24. S.Y. Xiang, Y.H. Zhang, J.K. Gong, X.X. Guo, L. Lin, Y. Hao, STDP-based unsupervised spike pattern learning in a photonic spiking neural network with VCSELs and VCSOAs. IEEE J. Sel. Top. Quantum Electron. **25**(6), 1700109 (2019)
25. Z.W. Song, S.Y. Xiang, Z.X. Ren, G.Q. Han, Y. Hao, Spike sequence learning in a photonic spiking neural network consisting of VCSELs-SA with supervised training. IEEE J. Sel. Top. Quantum Electron. **26**(5), 1700209 (2020)
26. S.Y. Xiang, Z.X. Ren, Z.W. Song, Y.H. Zhang, X.X. Guo, G.Q. Han, Y. Hao, Computing primitive of fully VCSEL-based all-optical spiking neural network for supervised learning and pattern classification. IEEE T Neur Net Lear. **32**(6), 2494–2505 (2021)
27. Y.H. Han, S.Y. Xiang, Z.X. Ren, C.T. Fu, A.J. Wen, Y. Hao, Delay-weight plasticity-based supervised learning in optical spiking neural networks. Photonics Res. **9**(4), 119–126 (2021)
28. S.Y. Xiang, Y.C. Shi, X.X. Guo, Y.H. Zhang, H.J. Wang, D.Z. Zheng, Z.W. Song, Y.N. Han, S.A. Gao, S.H. Zhao, B.L. Gu, H.L. Wang, X.J. Zhu, L.P. Hou, X.F. Chen, W.H. Zheng, X.H. Ma, Y. Hao, Hardware-algorithm collaborative computing with photonic spiking neuron chip based on an integrated fabry-perot laser with a saturable absorber. Optica. **10**(2), 162–171 (2023)
29. Y.H. Zhang, J. Robertson, S.Y. Xiang, M. Hejda, J. Bueno, A. Hurtado, All-optical neuromorphic binary convolution with a spiking VCSEL neuron for image gradient magnitudes. Photonics Res. **9**(5), 201–209 (2021)
30. J. Robertson, Y.H. Zhang, M. Hejda, J. Bueno, S.Y. Xiang, A. Hurtado, Image edge detection with a photonic spiking VCSEL-neuron. Opt. Express. **28**, 37526–37537 (2020)
31. S.Y. Xiang, Z.X. Ren, Y.H. Zhang, Z. Song, Y. Hao, All-optical neuromorphic XOR operation with inhibitory dynamics of a single photonic spiking neuron based on VCSEL-SA. Opt. Lett. **45**(5), 1104–1107 (2020)
32. Y. Lu, W.J. Zhang, B.Q. Fu, J.B. Du, Z.Y. He, Synaptic delay plasticity based on frequency-switched VCSELs for optical delay-weight spiking neural networks. Opt. Lett. **47**, 5587–5590 (2022)
33. N.C. Gerhardt, M.R. Hofmann, Spin-controlled vertical-cavity surface-emitting lasers. Adv. Opt. Photonics. **15**, 268949 (2012)
34. M. Holub, J. Shin, D. Saha, Electrical spin injection and threshold reduction in a semiconductor laser. Phys. Rev. Lett. **98**(14), 146603 (2007)
35. S. Hövel, N.C. Gerhardt, C. Brenner, M.R. Hofmann, F.Y. Lo, D. Reuter, A.D. Wieck, E. Schuster, W. Keune, Spin-controlled

LEDs and VCSELs. Phys. Status Solidi (A). **204**(2), 500–507 (2007)

36. N. Gerhardt, S. Hövel, M. Hofmann, J. Yang, D. Reuter, A. Wieck, Enhancement of spin information with vertical cavity surface emitting lasers. Electron. Lett. **42**(2), 88–89 (2006)
37. K. Schires, R. Al-Seyab, A. Hurtado, V.M. Korpijärvi, M. Guina, I.D. Henning, M.J. Adams, Optically-pumped dilute nitride spin-VCSEL. Opt. Express. **20**(4), 3550–3555 (2012)
38. S.S. Alharthi, A. Hurtado, V.M. Korpijarvi, M. Guina, I.D. Henning, M.J. Adams, Circular polarization switching and bistability in an optically injected 1300 nm spin-vertical cavity surface emitting laser. Appl. Phys. Lett. **106**(2), 021117 (2015)
39. S.S. Alharthi, A. Hurtado, R. Al-Seyab, V.M. Korpijarvi, M. Guina, I.D. Henning, M.J. Adams, Control of emitted light polarization in a 1310 nm dilute nitride spin-vertical cavity surface emitting laser subject to circularly polarized optical injection. Appl. Phys. Lett. **105**(18), 181106 (2014)
40. A. Dyson, M.J. Adams, Spin-polarized properties of optically pumped vertical cavity surface emitting lasers. J. Opt. B: Quantum Semiclass Opt. **5**(3), 222–226 (2003)
41. M. Torre, H. Susanto, N. Li, K. Schires, M.F. Salvide, I.D. Henning, M.J. Adams, A. Hurtado, High frequency continuous birefringence oscillations in spin-polarized vertical-cavity surface-emitting lasers. Opt. Lett. **42**(8), 1628–1631 (2017)
42. N. Yokota, K. Nisaka, H. Yasaka, K. Ikeda, Spin polarization modulation for high-speed vertical-cavity surface-emitting lasers. Appl. Phys. Lett. **113**(17), 171102 (2018)
43. M. Lindemann, G.F. Xu, T. Pusch, R. Michalzik, M.R. Hofmann, I. Zutic, N.C. Gerhardt, Ultrafast spin-lasers. Nature. **568**(7751), 212–215 (2019)
44. N.Q. Li, H. Susanto, B.R. Cemlyn, I.D. Henning, M.J. Adams, Secure communication systems based on chaos in optically-pumped Spin-VCSELs. Opt. Lett. **42**(17), 3494–3497 (2017)
45. N.Q. Li, H. Susanto, B.R. Cemlyn, I.D. Henning, M.J. Adams, Stability and bifurcation analysis of spin-polarized vertical-cavity surface-emitting lasers. Phys. Rev. A **96**(1), 013840 (2017)
46. N.Q. Li, D. Alexandropoulos, H. Susanto, I.D. Henning, M.J. Adams, Stability analysis of quantum-dot spin-VCSELs. Electronics. **5**(4), 83 (2016)
47. T.T. Song, Y.Y. Xie, Y.C. Ye, B.C. Liu, J.X. Chai, X. Jiang, Y.L. Zheng, Numerical analysis of nonlinear dynamics based on Spin-VCSELs with optical feedback. Photonics. **8**(1), 10 (2020)
48. R. Al-Seyab, D. Alexandropoulos, I.D. Henning, M.J. Adams, Instabilities in spin-polarized vertical-cavity surface-emitting lasers. IEEE Photonics J. **3**(5), 799–809 (2011)
49. Y.G. Yang, P. Zhou, P.H. Mu, N.Q. Li, Time-delayed reservoir computing based on an optically pumped spin VCSEL for high-speed processing. Nonlinear Dyn. **107**(3), 2619–2632 (2022)
50. S.Y. Xiang, H. Zhang, X.X. Guo, J.F. L, A.J. Wen, W. Pan, Y. Hao, Cascadable neuron-like spiking dynamics in coupled VCSELs subject to orthogonally polarized optical pulse injection. IEEE J. Sel. Top. Quantum Electron. **23**(6), 1700207 (2017)